

See discussions, stats, and author profiles for this publication at: <https://www.researchgate.net/publication/44067007>

# Substituent Effects on Dynamics at Conical Intersections: $\alpha,\beta$ -Enones

ARTICLE in THE JOURNAL OF PHYSICAL CHEMISTRY A · DECEMBER 2007

Impact Factor: 2.69 · DOI: 10.1021/jp074622j

CITATIONS

38

READS

55

10 AUTHORS, INCLUDING:



**Marek Zgierski**

National Research Council Canada

340 PUBLICATIONS 8,170 CITATIONS

SEE PROFILE



**I-Chia Chen**

National Tsing Hua University

97 PUBLICATIONS 1,493 CITATIONS

SEE PROFILE



**Todd J. Martinez**

Stanford University

238 PUBLICATIONS 7,665 CITATIONS

SEE PROFILE



**Albert Stolow**

University of Ottawa

177 PUBLICATIONS 5,145 CITATIONS

SEE PROFILE

Substituent Effects on Dynamics at Conical Intersections:  $\alpha,\beta$ -EnonesA. M. D. Lee,<sup>†,‡</sup> J. D. Coe,<sup>§</sup> S. Ullrich,<sup>#</sup> M.-L. Ho,<sup>||</sup> S.-J. Lee,<sup>||</sup> B.-M. Cheng,<sup>⊥</sup> M. Z. Zgierski,<sup>†</sup> I.-C. Chen,<sup>||</sup> T. J. Martinez,<sup>§</sup> and Albert Stolow<sup>\*,†,‡</sup>

Steacie Institute for Molecular Sciences, National Research Council, Ottawa, Ontario K1A 0R6, Canada, Department of Chemistry, Queen's University, Kingston, Ontario K7L 3N6, Canada, Department of Chemistry, University of Illinois at Urbana–Champaign, Urbana, Illinois 61801, Department of Chemistry, National Tsing-Hua University, Hsinchu, Taiwan 300, Republic of China, and National Synchrotron Radiation Research Center, Hsinchu, Taiwan 300, Republic of China

Received: June 14, 2007; In Final Form: August 21, 2007

Femtosecond time-resolved photoelectron spectroscopy and high-level theoretical calculations were used to study the effects of methyl substitution on the electronic dynamics of the  $\alpha,\beta$ -enones acrolein (2-propenal), crotonaldehyde (2-butenal), methylvinylketone (3-buten-2-one), and methacrolein (2-methyl-2-propenal) following excitation to the  $S_2(\pi\pi^*)$  state at 209 and 200 nm. We determine that following excitation the molecules move rapidly away from the Franck–Condon region, reaching a conical intersection promoting relaxation to the  $S_1(n\pi^*)$  state. Once on the  $S_1$  surface, the trajectories access another conical intersection, leading them to the ground state. Only small variations between molecules are seen in their  $S_2$  decay times. However, the position of methyl group substitution greatly affects the relaxation rate from the  $S_1$  surface and the branching ratios to the products. Ab initio calculations used to compare the geometries, energies, and topographies of the  $S_1/S_0$  conical intersections of the molecules are not able to satisfactorily explain the variations in relaxation behavior. We propose that the  $S_1$  lifetime differences are caused by specific dynamical factors that affect the efficiency of passage through the  $S_1/S_0$  conical intersection.

## 1. Introduction

Conical intersections (CIs) continue to find increasing importance in descriptions of nonadiabatic dynamics in excited states of polyatomic molecules.<sup>1–3</sup> They can lead to very fast electronic relaxation dynamics (internal conversion) on the femtosecond and picosecond timescales. The literature contains numerous examples where the discovery of a CI in a polyatomic molecule leads to conclusions being drawn about its excited-state chemical dynamics and branching ratios. Yet, merely finding a CI does not indicate how or even if a molecular trajectory passes near it.

Consideration of CIs as important features on potential energy surfaces (PESs) is dependent on a number of factors. The first, trivial concern is whether or not the CI is conformationally and energetically accessible from the initially excited state. The energy of the CI may be important, particularly when the CI is located above an excited-state minimum and the molecule relaxes to this minimum before internal conversion occurs. In this case, the energy difference between the minimum and the CI represents an effective barrier over which the molecular trajectory must pass. Analogous to the behavior of a barrier in statistical transition state theory, CIs with low barriers generally have faster relaxation rates than those with large barriers. Closely related is the amount of excess energy available to reach the

CI. Molecules with large amounts of excess internal energy are expected to have faster nonadiabatic relaxation through CIs than those with little excess energy. The topography (tilt and asymmetry) of the CI is also important. Atchity et al.<sup>4</sup> and Yarkony<sup>3</sup> have examined CIs and classified them into two categories: “peaked” and “sloped”. Peaked topographies lead to fast internal conversion by funneling the trajectories toward the CI, while trajectories that do make it through sloped topographies have some likelihood to recross back onto the upper state, leading to slower net internal conversion. Ben-Nun and Martinez<sup>2</sup> have used this reasoning to explain the selectivity of cis–trans isomerization about the  $C_{11}$  double bond versus the  $C_{13}$  double bond in retinal. Often overlooked but arguably equally important to the topographical features of the potential energy surface are dynamical factors affecting excited-state trajectories. By dynamical factors, we mean specific molecular motions (both their magnitude and speed) that promote or hinder nonadiabatic crossing of the excited-state trajectory. Similar to the one-dimensional avoided crossing surface hopping probability analyses of Landau and Zener,<sup>5,6</sup> the velocity of the trajectory near a CI is expected to affect the branching ratio between adiabatic and nonadiabatic dynamics.

Here we use methyl substitution to investigate its effect on the time scales of ultrafast nonadiabatic processes in the simplest  $\alpha,\beta$ -enones using time-resolved photoelectron spectroscopy (TRPES).<sup>7–9</sup> We attempt to rationalize the different observed dynamical time scales between the molecules using high-level theoretical calculations to analyze the structures and energies of the ground and important excited states. In addition, we map the topographies of the conical intersections relevant to the dynamics that we observe. The ultimate goal of this research is to help develop a theory that incorporates the elements of CI

\* Author to whom correspondence should be addressed. E-mail: albert.stolow@nrc.ca.

<sup>†</sup> National Research Council.

<sup>‡</sup> Queen's University.

<sup>§</sup> University of Illinois at Urbana–Champaign.

<sup>||</sup> National Tsing-Hua University.

<sup>⊥</sup> National Synchrotron Radiation Research Center.

<sup>#</sup> Current address: Department of Physics, University of Georgia, Athens, Georgia 30602.

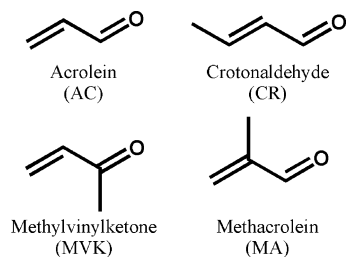


**Figure 1.**  $\alpha,\beta$ -Enones: acrolein, crotonaldehyde, methylvinylketone, and methacrolein.

energetics, CI topography, and dynamical factors near CIs to explain and predict nonadiabatic excited-state dynamics in polyatomic molecules.

The  $\alpha,\beta$ -enones contain the conjugated  $-C=C-C=O$  chromophore. Unlike the conjugated hydrocarbons, additional excited states exist, and different photochemical pathways are available due to the presence of the nonbonding electrons on the oxygen atom. The simplest  $\alpha,\beta$ -enone, acrolein (AC), is an important theoretical system for quantitatively studying configuration interaction with dynamic electron correlation effects. The PES landscape of AC is predicted to abound with conical intersections and intersystem crossings (ISCs) that control the excited-state relaxation pathways.<sup>10–12</sup> We compare the dynamics of AC with its singly methyl-substituted analogues crotonaldehyde (CR), methylvinylketone (MVK), and methacrolein (MA). These molecules are depicted in Figure 1.

In the ground state, conjugation across the central C–C bond restricts internal rotation, and AC is found to have a planar s-trans structure at room temperature. A strong, broad electronic transition at 193 nm (6.4 eV) is attributed to the  $S_2(\pi\pi^*)$  state while weak transitions at 387 nm (3.2 eV) and 412 nm (3.0 eV) have been assigned to the  $S_1(n\pi^*)$  and  $T_1(n\pi^*)$  states, respectively.<sup>13</sup>

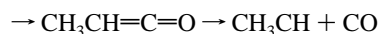
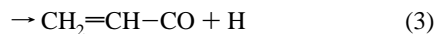
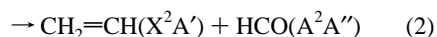
The  $S_2 \leftarrow S_0$  absorption in AC is qualitatively the transition of an electron from the bonding  $\pi$  orbital to the antibonding  $\pi^*$  orbital. As expected from symmetry considerations, this transition has a large oscillator strength. A simple molecular orbital analysis indicates that this state is biradicaloid in nature with significant bond reversal relative to the ground state, strengthening the central C–C bond and weakening the C=C and C=O double bonds. Treatment of dynamical electron correlation is required to calculate the vertical excitation energies accurately.<sup>14</sup> Theoretical studies predict that the bond reversal in this excited state results in the minimum energy geometry having the terminal  $CH_2$  group rotated out of plane by approximately  $90^\circ$ .<sup>10,11,14</sup>

The  $S_1$  electronic state in AC is approximately the ground-state configuration with a nonbonding electron on oxygen ( $n_O$ ) removed and placed in the  $\pi^*$  orbital. Forbidden by orbital symmetry considerations, this transition has little oscillator strength. Bond order reversal is expected, although to a lesser extent than that in  $S_2$  because only one electron occupies the antibonding  $\pi^*$  orbital whereas two occupy the bonding  $\pi$  orbital. Charge reversal along the C=O bond is also expected with the oxygen becoming more positively charged because the  $n_O$  electron nominally residing on oxygen is delocalized into the  $\pi$ -system. Bond length increases of  $\sim 0.12$  Å for the C=C and C=O bonds were observed spectroscopically after excitation to the  $S_1$  state.<sup>13,15,16</sup> Detailed studies of the vibronic spectra of the  $S_1$  state were performed on AC<sup>16–19</sup> and CR, MVK, and MA.<sup>20</sup> Unlike the other molecules, MA shows richer structure in its  $S_1$  vibronic spectrum due to a series of C=C vibrational bands.

In AC, the ordering of the lowest triplet states ( $^3n\pi^*$  and  $^3\pi\pi^*$ ) depends on geometry. For vertical excitation from the ground state,  $^3n\pi^*$  is the lowest state. However, by twisting the terminal  $CH_2$  to  $\sim 90^\circ$ , the triplet states are nearly degenerate, with the  $^3\pi\pi^*$  state slightly lower in energy.<sup>11,14</sup> The minimum energy conformations of both triplet states lie below the  $S_1$  minimum energy.

At 193 nm, the AC  $S_2$  state adiabatically correlates with energetically unavailable, highly excited dissociation products and, therefore, is assumed to rapidly internally convert to the lower lying singlet state,  $S_1$ .<sup>11,21</sup> Reguero et al.<sup>10</sup> suggest three possible relaxation mechanisms from  $S_1$ : internal conversion to  $S_0$  from a  $\sim 90^\circ$  twisted  $S_1$  state, fluorescence from the  $S_1$  minimum to the ground state, or ISC to the triplet manifold, with  $T_2(\pi\pi^*) \leftarrow S_1(n\pi^*)$  being the dominant channel according to El-Sayed's Rules.<sup>22</sup>

Numerous researchers have performed laser photodissociation experiments at 193 nm on AC<sup>21,23–25</sup> and CR.<sup>27</sup> Photodissociation experiments near 300 nm have also been performed on AC in the gas phase<sup>28</sup> and in argon matrixes.<sup>29</sup> Following 193 nm photoexcitation to the  $S_2$  state in AC, the main fragmentation pathways are



The most extensive ab initio electronic structure calculations on AC to date have been conducted by Fang.<sup>11</sup> The  $HCO(X^2A')$  product channel (eq 1) was found to correlate directly with the ground and  $^3\pi\pi^*$  states, while the  $HCO(A^2A'')$  product channel correlates with  $S_1$ . However, the  $HCO(A)$  state is predissociative on the picosecond time scale<sup>30</sup> and is not easily detectable using laser or mass spectrometric techniques. The molecular CO formation channel (eq 4) is believed to occur via a 1,3-H sigmatropic shift on the  $^3\pi\pi^*$  surface followed by fragmentation and rearrangement.

## 2. Experimental Section

**2.1. Vacuum UV Absorption Spectra.** Absolute absorption cross-sections of AC, CR, and MA were measured using synchrotron radiation from the HF-CGM beamline at the National Synchrotron Radiation Research Center in Hsinchu, Taiwan. This beamline is equipped with a cylindrical grating (600 lines/mm, focal length of 6 m, and variable slit width) for usage in the wavelength range of 105–230 nm. A LiF window eliminated short-wavelength, high-order light diffracted from the grating. A double-beam absorption cell of 8.9 cm in length simultaneously recorded the incident and transmitted light intensities to obtain the absorbance. The samples were purified at least twice via vacuum distillation prior to use. The absolute wavelength positions were calibrated with lines of CO, NO, and  $O_2$  in the same wavelength region.

The UV absorption spectra of AC, CR, and MA are shown in Figure 2. The UV absorption spectrum of MVK has been reported previously.<sup>31,32</sup> AC was measured with 0.1 nm resolution between 223 and 177 nm and 0.02 nm resolution between 177 and 105 nm. CR was measured with 0.1 nm resolution between 230 and 184.5 nm and 0.02 nm resolution between 184.5 and 105 nm. MA was measured with 0.1 nm resolution

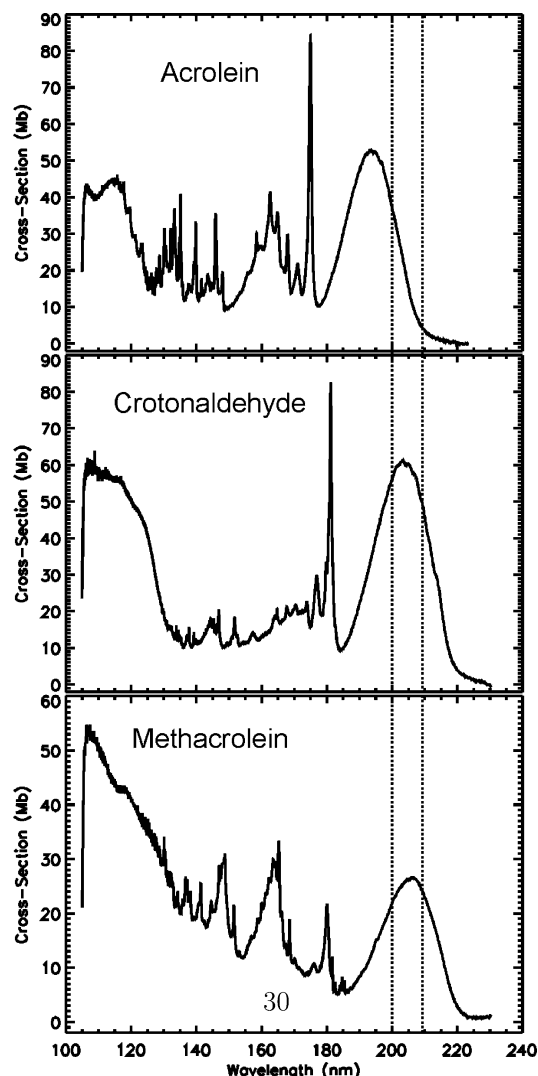


**Figure 2.** Absolute UV absorption cross-sections of acrolein, crotonaldehyde, and methacrolein measured with synchrotron radiation. Acrolein was measured with 0.1 nm resolution between 223 and 177 nm and 0.02 nm resolution between 177 and 105 nm. Crotonaldehyde was measured with 0.1 nm resolution between 230 and 184.5 nm and 0.02 nm resolution between 184.5 and 105 nm. Methacrolein was measured with 0.1 nm resolution between 230 and 190 nm, 0.02 nm resolution between 190 and 129 nm, and 0.05 nm resolution between 129 and 105 nm. The excitation wavelengths (200 and 209 nm) used in the time-resolved photoelectron experiments are indicated by dotted lines.

between 230 and 190 nm, 0.02 nm resolution between 190 and 129 nm, and 0.05 nm resolution between 129 and 105 nm. The broad, featureless absorption band of the  $S_2$  state can be seen near 200 nm in all cases. The excitation wavelengths used in the time-resolved experiments (200 and 209 nm) are indicated by dotted lines in the figures.

**2.2. Time-Resolved Photoelectron Spectroscopy.** We briefly describe our femtosecond time-resolved magnetic bottle photoelectron spectrometer experiments, as detailed elsewhere.<sup>33</sup> Harmonic generation of an amplified femtosecond Ti:sapphire system was used to produce pump and probe laser pulses for two complete sets of experiments: one using 209 nm pump and 279 nm probe pulses; the other using 200 nm pump and 267 nm probe pulses. The UV pulses were individually recompressed using  $\text{CaF}_2$  prism pairs, combined collinearly, and then gently focused using  $f/80$  spherical reflective optics to intersect a seeded molecular beam in the interaction region of a magnetic bottle spectrometer. Time delays between pump

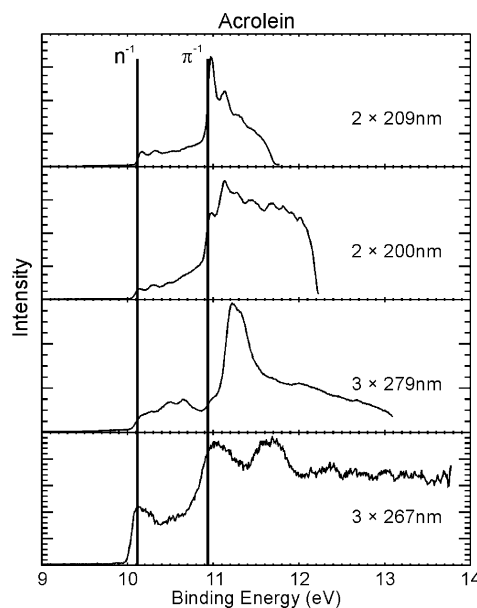


**Figure 3.** Multiphoton photoionization spectra of acrolein. The energy axis is labeled for two-photon ionization at 200 and 209 nm and three-photon ionization at 267 and 279 nm. The He(I) photoionization energies from the  $n$  and  $\pi$  orbitals are indicated with vertical lines.

and probe pulses were scanned using a computer-controlled stepper motor in 25 fs steps. Typically, pump pulse energies were  $\sim 100$  nJ, and probe pulse energies were  $\sim 2.5$   $\mu$ J. Supersonic molecular beams of AC, CR, MVK, and MA were made by bubbling helium through the respective neat liquid. The liquids were precooled in a temperature-controlled bath to choose a desired vapor pressure. The 200 or 209 nm pump pulse excited the molecules from their  $S_0$  ground state into their  $S_2$  ( $\pi\pi^*$ ) excited state. The delayed 267 or 279 nm probe pulse produced photoelectrons via one- and/or two-photon ionization of the excited molecule. Photoelectron spectra arising from the pump laser alone and probe laser alone were subtracted to correct for background photoelectrons generated from single-color multiphoton ionization. For each particular molecule, the pump–probe time delays were scanned back and forth multiple times to minimize any effects of temporal and/or spatial laser drift.

The electron kinetic energy calibration and time zero overlap of the two laser pulses were achieved using the well-characterized  $1 + 1'$  photoionization of nitric oxide. Measured  $1 + 1'$  pump–probe cross-correlations (i.e., instrumental response or time resolution) ranged between 150 and 170 fs. The energy and time calibration scans were performed both before and after each experiment.

Single-color multiphoton photoelectron spectra at 209 nm ( $2 \times 5.93$  eV = 11.86 eV), 200 nm ( $2 \times 6.2$  eV = 12.4 eV), 279 nm ( $3 \times 4.44$  eV = 13.32 eV), and 267 nm ( $3 \times 4.65$  eV = 13.95 eV) for AC, CR, MVK, and MA are shown in Figures 3–6, respectively. As determined by He(I) photoelectron spectroscopy, the  $n$ -hole and  $\pi$ -hole ionization energies for the molecules are:<sup>34</sup> AC (10.11 and 10.93 eV), CR (9.75 and 10.20 eV), MVK (9.66 and 10.53 eV), and MA (9.92 and 10.38 eV). Due to the resonant nature of the multiphoton ionization process ( $1 + 1$  for 209/200 nm and  $2 + 1$  for 279/267 nm), bands are present in the 11–12 eV region not seen previously in the one-photon He(I) spectra.<sup>34–36</sup> The shapes of the spectra from our experiments are determined by fast dynamics of the molecules occurring within the duration of the laser pulses. Rapid, large-amplitude motions of the molecules allow ionization to ionic states with geometries different from

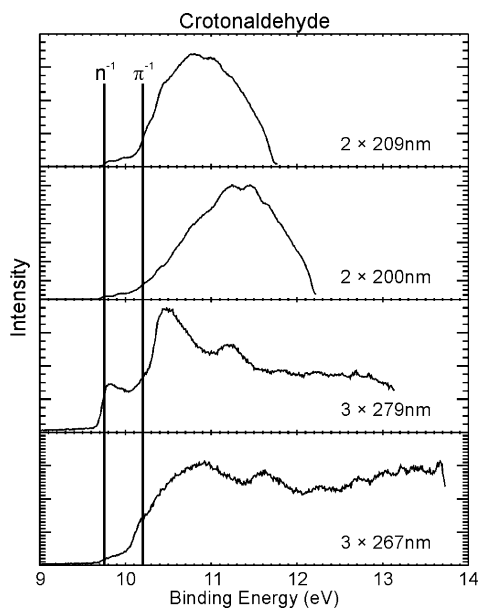


**Figure 4.** Multiphoton photoionization spectra of crotonaldehyde. The energy axis is labeled for two-photon ionization at 200 and 209 nm and three-photon ionization at 267 and 279 nm. The He(I) photoionization energies from the  $n$  and  $\pi$  orbitals are indicated with vertical lines.

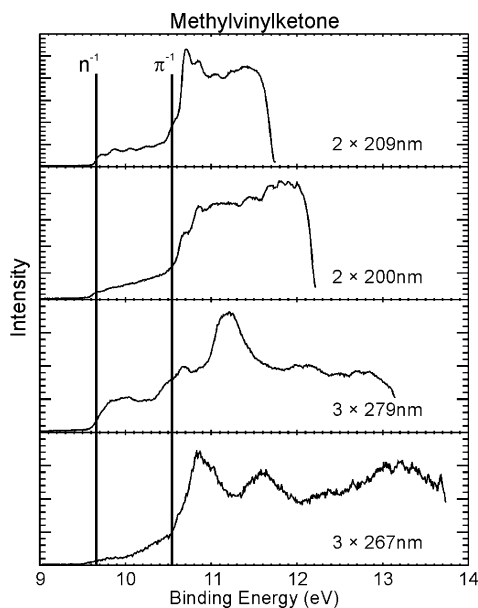


**Figure 5.** Multiphoton photoionization spectra of methylvinylketone. The energy axis is labeled for two-photon ionization at 200 and 209 nm and three-photon ionization at 267 and 279 nm. The He(I) photoionization energies from the  $n$  and  $\pi$  orbitals are indicated with vertical lines.

that of the ground state. Ionic state energies ( $D_0$ , ...,  $D_4$ ) calculated at the TD/B3LYP/cc-pvdz level of theory using  $D_0$ -optimized geometries are shown in Table 1. The ordering of the ionization energies between the molecules is predicted correctly when compared to experiment. The presence of ionic states in the 11–12 eV region agrees with our measured photoelectron spectra.

**2.3. Ab Initio Calculations.** Excited-state geometries were optimized using the complete active space self-consistent field (CASSCF)<sup>37</sup> method with a (6,5) active space. To optimize the states in an equivalent manner, the orbitals were optimized to yield the lowest average energy for the first three singlet states, using the state-averaged<sup>38</sup> approach (SA3-CAS). Ground-state

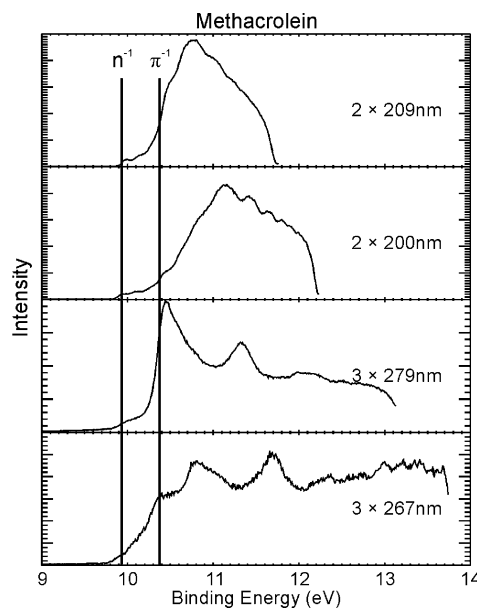


**Figure 6.** Multiphoton photoionization spectra of methacrolein. The energy axis is labeled for two-photon ionization at 200 and 209 nm and three-photon ionization at 267 and 279 nm. The He(I) photoionization energies from the  $n$  and  $\pi$  orbitals are indicated with vertical lines.

**TABLE 1: Energies of Ionic States Optimized at the  $D_0$  Geometry Using the TD/B3LYP/cc-pvdz Level of Theory<sup>a</sup>**

state	AC	CR	MVK	MA
$D_0$	9.78 (10.11)	9.29 (9.75)	9.26 (9.66)	9.56 (9.92)
$D_1$	10.62 (10.93)	9.78 (10.20)	10.28 (10.53)	9.93 (10.38)
$D_2$	12.84	12.37	12.40	12.28
$D_3$	13.46	12.49	12.84	12.31
$D_4$	13.80	13.09	12.50	12.63

<sup>a</sup> Values obtained from the literature for He(I) photoionization are shown in parentheses.<sup>34</sup> The energies are reported in electronvolts and are Relative to the neutral ground state.

geometries were minimized at the MP2 level. All calculations employed a 6-31G\* basis set and were performed with the MOLPRO suite.<sup>39</sup>

The optimized geometries for the  $S_0$  and  $S_1$  minima and the minimum energy conical intersection (MECI) points connecting  $S_2$  with  $S_1$  and  $S_1$  with  $S_0$  are shown in Figures 7–9, respectively. The energies of these structures are shown in Table 2. Attempts to locate a true minimum with all real vibrational frequencies on  $S_2$  were unsuccessful. Bond alternation progresses smoothly from  $C=C-C=O$  at the  $S_2$  Franck–Condon (FC) point, to a resonant pattern in which all three bond lengths are roughly equal at the  $S_1$  minimum, to full reversal as  $C-C=C-O$  at the  $S_1/S_0$  MECI. The geometries of all of the calculated structures are shown in the Supporting Information.

The four molecules have very similar geometries at the ground state ( $S_0$ ) minimum, the  $S_1$  minimum, and the  $S_2/S_1$  and  $S_1/S_0$  MECIs. All are planar at the  $S_0$  and  $S_1$  minima but twisted and pyramidalized to roughly the same degree at the  $S_1/S_0$  MECI. Pyramidalization is a common feature of intersection geometries.<sup>2,40,41</sup> The pyramidalization angles indicated in Figure 9 are defined as

$$\tau_{\text{pyr}} = \cos^{-1}((\mathbf{e}_{C_p R_1} \times \mathbf{e}_{C_p R_2}) \cdot \mathbf{e}_{C_p C_2}) - \frac{\pi}{2} \quad (5)$$

where unit vectors pointing along a bond from atom A to atom B are denoted by  $\mathbf{e}_{AB}$ . The  $S_2/S_1$  MECI geometries vary to a



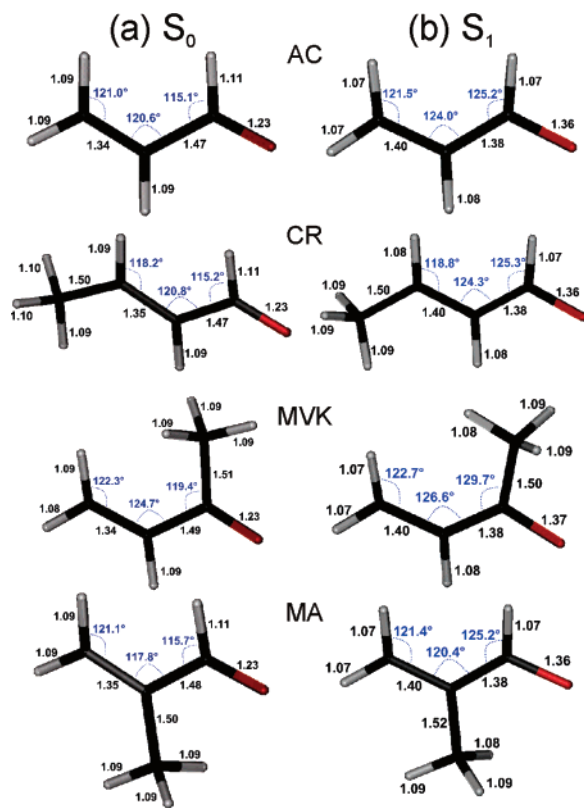


**Figure 7.** (a) MP2/6-31G\*  $S_0$  minima and (b) SA3-CAS(6,5)/6-31G\*  $S_1$  minima structures of the  $\alpha,\beta$ -enones. Apart from the methyl groups, all of the structures are planar.

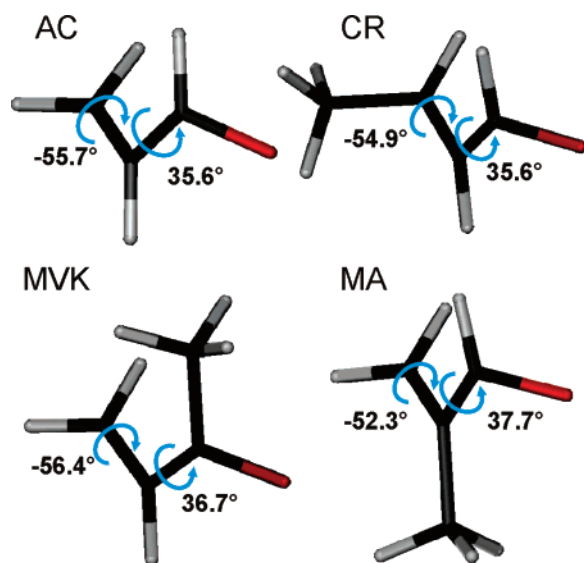


**Figure 8.** SA3-CAS(6,5)/6-31G\*  $S_2/S_1$  minimum energy conical intersection structures for the  $\alpha,\beta$ -enones studied here. All four molecules are twisted about both C–C bonds of the molecular backbone. The torsional angles indicated are the average values for all dihedral angles about the  $C_1-C_2$  bond. These are explicitly defined in the Supporting Information.

slightly larger extent than the other points, but all are twisted along the carbon backbone.

### 3. Results and Discussion

Excerpts from the time-resolved photoelectron scans at selected pump–probe time delays are shown in Figures 10 and 11. Each time delay in the plot is offset vertically downward as the pump–probe time delay increases. The scans start from

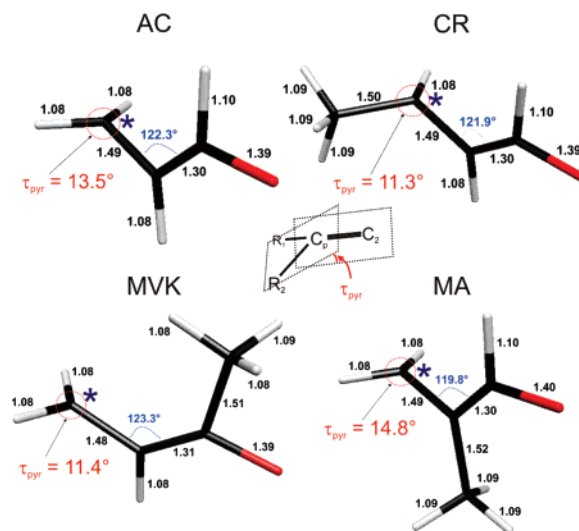


**Figure 9.** SA3-CAS(6,5)/6-31G\*  $S_1/S_0$  minimum energy conical intersection structures for the  $\alpha,\beta$ -enones studied here. Structures are twisted  $90^\circ$  about the nominally C=C bond, and the terminal carbon is slightly pyramidalized in all four cases. The twisted bonds are labeled with asterisks. The pyramidalization angle  $\tau_{pyr}$  is explicitly defined in the text.

**TABLE 2: SA3-CAS(6,5)/6-31G\* Calculated Energies for the Franck–Condon Vertical Excitation to  $S_2$  ( $S_2$  FC), the  $S_2/S_1$  MECI, the  $S_1$  Minimum, and the  $S_1/S_0$  MECI of the  $\alpha,\beta$ -Enones Examined in the Text<sup>a</sup>**

	$S_2$ FC	$S_2/S_1$ CI	$S_1$ min	$S_1/S_0$ CI
AC	7.55 (6.41)	5.38	2.96 (3.21) <sup>20</sup>	3.94
CR	6.92 (6.11)	5.32	2.90 (3.29) <sup>20</sup>	3.89
MVK	6.98 (6.36) <sup>31</sup>	5.34	2.93 (3.24) <sup>20</sup>	3.75
MA	6.96 (6.00)	5.29	2.98 (3.28) <sup>20</sup>	3.80

<sup>a</sup> Experimental values are shown in parentheses. All energies are relative to the ground state and reported in electronvolts.

0.2 eV because the magnetic bottle transmission below this energy is unreliable.

For the 209 + 279 nm experiments, the  $1 + 1'$  and  $1 + 2'$  total photon energies are 10.38 and 14.81 eV, respectively. Likewise, for the 200 + 267 nm experiments, the total photon energies are 10.85 and 15.50 eV. Thus, there are two regions in the photoelectron spectra, resulting from ionization via these two processes. In the low electron kinetic energy region of the spectra, photoelectrons are produced from both types of pump–probe processes: single photon ionization of the excited states by the probe laser ( $1 + 1'$ ) and two-photon ionization by the probe laser ( $1 + 2'$ ). In the high electron kinetic energy region of the spectra, all photoelectrons result from  $1 + 2'$  ionization.

As a first step in the analysis, the photoelectron energy/time delay scans were sliced into 0.025 eV bins to yield time-dependent transients. Each time transient was fit using an exponential kinetic model convoluted with the appropriate Gaussian instrumental response function. In the  $1 + 1'$  region, the instrumental response was taken to be the Gaussian fit of the measured NO  $1 + 1'$  cross-correlation with full width at half-maximum  $\tau_{1+1'}$ . In the  $1 + 2'$  region of the spectra, the pump and probe laser pulses were assumed to be of the same duration such that the  $1 + 2'$  instrumental response  $\tau_{1+2'}$  could be calculated using  $\tau_{1+2'} = \tau_{1+1'}\sqrt{3/2}$ .

The time constants and spectral amplitudes were varied to minimize the weighted  $\chi^2$  value of the fit to the data. Initially, the time constants were allowed to vary independently from slice to slice. In all slices, for all molecules, it was found that the simplest model to fit all the time transients reasonably was

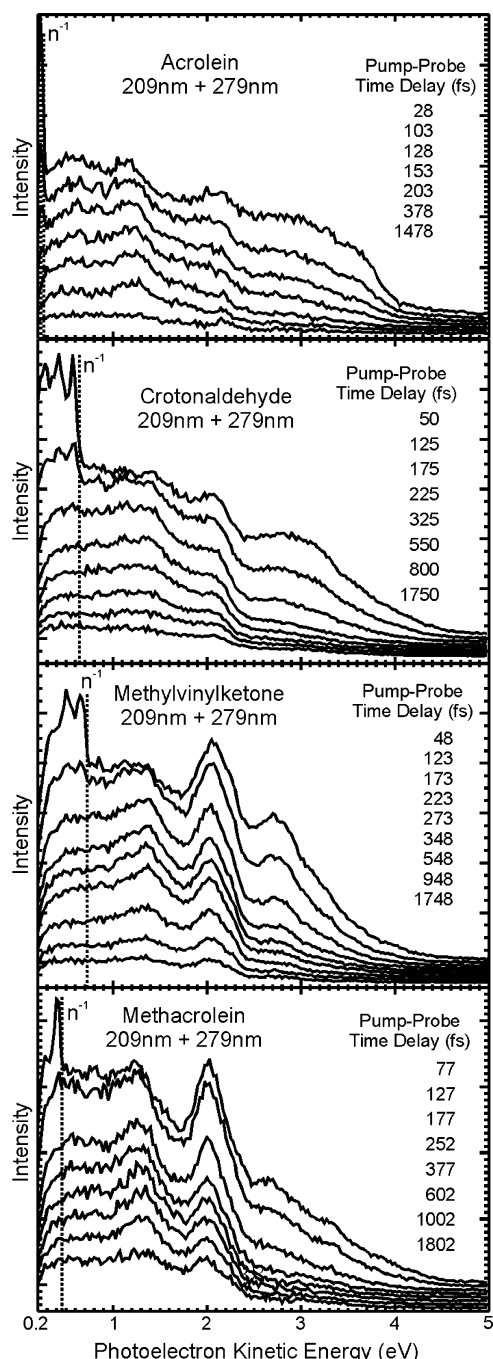


**Figure 10.** Selected time-dependent photoelectron spectra for acrolein, crotonaldehyde, methylvinylketone, and methacrolein using 209 nm pump and 279 nm probe pulses. Each time spectrum is offset downward with increasing time delay. The  $1 + 1'$   $n$ -hole ionization energies are shown as dotted vertical lines.

one that contained four components. One component, referred to here as  $X$ , was only present during the cross-correlation of the two laser pulses. The other three components were fit according to a sequential decay kinetic model in which an immediately prepared component  $A$  decayed with time constant  $t_1$  to an intermediate component  $I$ , which in turn decayed with time constant  $t_2$  to a product component  $P$ .

AC, MVK, and MA were found to have  $t_2$  values approximately constant across the entire photoelectron spectrum using both excitation/probing schemes. To fit  $t_2$  more accurately for these molecules, photoelectron spectra at short pump-probe delay times were removed to yield time transients consisting of only the  $I$  and  $P$  components. A global fitting procedure then

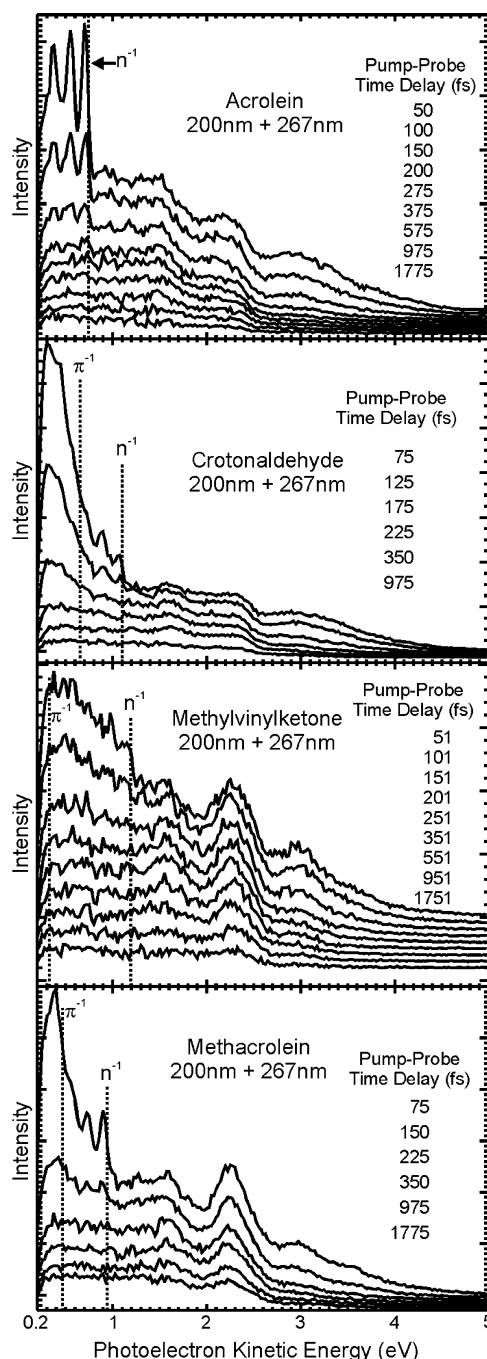


**Figure 11.** Selected time-dependent photoelectron spectra for acrolein, crotonaldehyde, methylvinylketone, and methacrolein using 200 nm pump and 267 nm probe pulses. Each time spectrum is offset downward with increasing time delay. The  $1 + 1'$   $n$ -hole and  $\pi$ -hole ionization energies are shown as dotted vertical lines.

was used in which  $t_2$  was optimized but held constant across the entire spectrum. The complete time transient was then refit with all components ( $X$ ,  $A$ ,  $I$ , and  $P$ ), this time holding  $t_2$  constant at the value from the previous analysis step. In contrast to the fitting of  $t_2$ ,  $t_1$  was found to vary across the spectrum for all molecules. This is indicative of large-amplitude motion occurring on this time scale. Nevertheless, in subregions of the spectra, the  $t_1$  values were found to be relatively constant. In these subregions, each roughly encompassing broad spectral features, the time transients were integrated, and the resulting transient was fit once again for  $t_1$  and the spectral amplitude. An example of one of the fits, for AC, is shown in Figure 12.

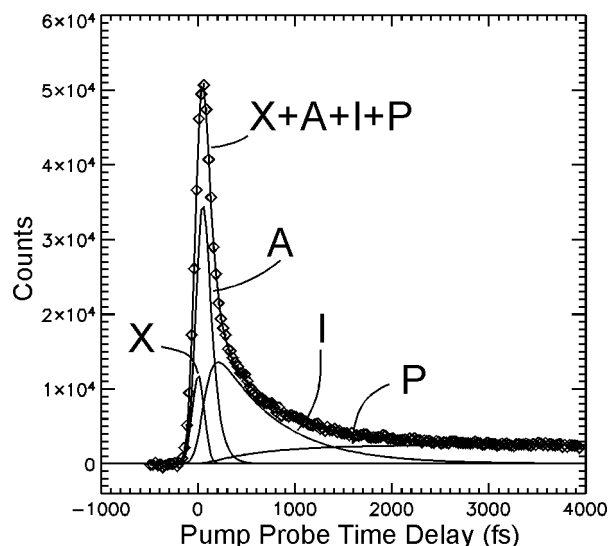


**Figure 12.** Example fit of acrolein 209 nm pump/279 nm probe data between 1.5 and 2.5 eV using a four-component sequential model: an instrumental response component *X*, an immediately excited species *A*, which decays to an intermediate *I*, which in turn decays to a product *P*. The decay times of the *A* and *I* components are 65 and 900 fs, respectively.

**TABLE 3: Fitted Time Constants for TRPES Scans of Acrolein, Crotonaldehyde, Methylvinylketone, and Methacrolein Using 209 nm Pump and 279 nm Probe Wavelengths<sup>a</sup>**

	energy range (eV)	$t_1$ (fs)	$t_2$ (fs)
AC	0.23–0.28	90 ± 20	900 ± 100
	0.28–1.5	100 ± 20	
	1.5–2.5	65 ± 25	
	2.5–5.0	45 ± 25	
CR	0.25–0.65	70 ± 30	380 ± 50
	0.65–2.4	90 ± 30	
	2.4–5.0	50 ± 15	
MVK	0.30–0.73	170 ± 20	1080 ± 80
	0.73–1.7	190 ± 30	
	1.7–2.6	140 ± 40	
	2.6–5.0	90 ± 20	
MA	0.30–0.46	150 ± 20	2020 ± 80
	0.46–1.7	150 ± 30	
	1.7–2.4	90 ± 20	
	2.4–5.0	70 ± 20	

<sup>a</sup> The model used to fit the spectra consisted of a cross-correlation response *X*, an immediately excited species *A* that decays with time constant  $t_1$  to intermediate *I*, which in turn decays with time constant  $t_2$  to product *P*.

For CR, the dynamics were sufficiently fast such that the time transients could not be fit with time constants in the piecewise fashion described above for the other molecules. In addition, both  $t_1$  and  $t_2$  were found to vary across the photoelectron spectrum, so no global fitting procedure could be applied, indicating that CR in some way behaves differently from the other molecules. The full energy range was divided into three subregions where  $t_1$  and  $t_2$  were approximately constant. Within these regions, the spectral slices were integrated, and the transient was fit again for  $t_1$ ,  $t_2$ , and the spectral amplitudes.

The time constants and spectral amplitudes for all molecules are summarized in Tables 3 (209 nm pump/279 nm probe) and 4 (200 nm pump/267 nm probe). The spectral amplitudes are determined such that direct comparisons should only be made

for individual species across the different energy regions, not between species within a single energy region. The time constants for  $t_1$  are comparable or shorter than the instrumental response yet are still easily observed and fit as seen in Figure 12. Uncertainty in the pump–probe overlap time and limitations in the Gaussian instrumental response function approximation results in large error bars for the values of  $t_1$ .

The validity and implications of this fitting model should be discussed. It is always possible to achieve a better fit by adding more components to the fitting procedure. Therefore, to justify this model over a three-component model, it is necessary to provide spectral evidence for four identifiable components. Simply adding components until an “acceptable” fit is achieved is not a satisfactory method to determine the number of components.

The product component *P* is easily distinguished because, at long time delays, it is the only component remaining after all other components have decayed to zero. It should be noted that labeling it as the product component does not mean that this species is stable indefinitely: It only means that it does not decay appreciably on the time scale of our experiment (i.e., approximately hundreds of picoseconds).

The instrumental response component *X* is also easily recognized because it follows the laser cross-correlation. The only part of the spectrum where the *X* component has significant amplitude is in the low-energy region where  $1 + 1'$  ionization dominates. Small *X* amplitudes in the  $1 + 2'$  region are most likely due to the limitations of fitting with a Gaussian laser cross-correlation. The  $1 + 1'$  ionization regime is the only region of the spectrum where the C–C stretching vibrations are resolved. The *X* component can arise from either resonant or nonresonant ionization of the molecules. If nonresonant ionization is primarily responsible for the spectra, then they should resemble the He(I) photoelectron spectra,<sup>34–36</sup> where  $n$ -hole and  $\pi$ -hole photoelectron bands are approximately equal in intensity with one or two vibration bands visible. However, the 200 nm spectra obtained here (Figure 11) show that the *X* components for the molecules are quite different in appearance from the He(I) spectra, with several vibrational bands seen in AC and  $\pi$ -hole ionization much more favored than  $n$ -hole ionization in CR and MA. If the ionization process resonantly involves the  $\pi\pi^*$  state, then we would expect that ionization correlates to the  $\pi$ -hole ionic state. The change in ionization propensity to favor  $\pi$ -orbital ionization can also be seen in the pump only ( $2 \times 200$  nm and  $2 \times 209$  nm) spectra in Figures 3–6. These single-color spectra can be thought of as a pump–probe experiment using 200 nm for both pump and probe pulses with a very short time delay between them. These compelling reasons provide strong evidence that the *X* component is a resonant signal and is part of the excited-state dynamical process.

The remaining components *A* and *I* are more difficult to separate because they are spectrally broad and overlap to a large extent. However, the global fitting procedure described above reveals significant differences in the spectra of the *A* and *I* components. Specifically, the *A* component has a larger contribution in the high electron kinetic energy region than the *I* component. Thus, we conclude that because the two components have different photoelectron spectra, they arise from ionization of two different electronic states.

It is important to state that this four-component sequential model is limited in several ways. It is constructed with exponential kinetics convoluted with fitted  $1 + 1'$  or  $1 + 2'$  Gaussian cross-correlations. The real measured  $1 + 1'$  cross-correlation can be used in some regions when convoluting with



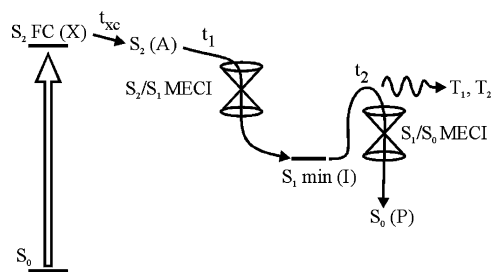


**Figure 13.** Proposed scheme for ultrafast  $S_2$  relaxation of the  $\alpha,\beta$ -enones.  $X$  is the Franck–Condon region on the  $S_2$  surface,  $A$  is away from the Franck–Condon region on the  $S_2$  surface,  $I$  is the  $S_1$  state, and  $P$  is the long-lived ( $>100$ s of picoseconds) hot ground-state or triplet-state products. The decay of  $X$  to  $A$  is very fast (i.e.,  $\ll 160$  fs, our laser cross-correlation).  $t_1$  and  $t_2$  are the decay times for  $A$  and  $I$ , respectively.

the exponential dynamics, but this correction is minor. The assumption of exponential dynamics is the more restrictive assumption, especially at short pump–probe delay times that are on the time scale of molecular vibrations. In addition, there is a somewhat hidden restriction implied by fitting the  $X$  component. By fitting it with the instrumental response function, it is equivalent to fitting an initially excited component that decays instantaneously with zero lifetime. It would be ideal to be able to relax this restriction because all resonant processes have some nonzero lifetime, however small. Yet this restriction is necessary because the observed  $t_1$  values are shorter or on the order of the instrumental response function ( $\sim 160$  fs). Regardless of the fitting procedure, two time constants cannot be fit that are close together (i.e., the same order of magnitude). Thus, the  $t_1$  values are probably the upper limit for the  $A \rightarrow I$  process.

For the above reasons, we conclude that the four-component fitting model used in this work describes a resonant process that starts with  $X$  decaying very rapidly to  $A$ , which decays with a maximum time constant  $t_1$  to  $I$ , which subsequently decays with time constant  $t_2$  to  $P$ . As detailed below, we propose the relaxation pathway from  $S_2$  for the  $\alpha,\beta$ -enones shown in Figure 13. In this scheme, relaxation rapidly occurs from the  $S_2$  FC region ( $X$ ) toward the  $S_2/S_1$  MECI. We assign the decay time  $t_1$  of component  $A$  to the residence time on the  $S_2$  surface. Fast internal conversion through a conical intersection leads the molecules onto the  $S_1$  surface ( $I$ ). From this surface, the molecules proceed through another conical intersection to produce hot ground-state molecules or intersystem cross to long-lived states in the triplet manifold. These “products” are the TRPES component identified as  $P$ .

The pump laser initially excites the planar ground-state molecules into the FC region of the  $S_2(\pi\pi^*)$  PES. The molecules are expected to move rapidly away from the FC region toward the more energetically favored geometries via torsion about the terminal  $\text{CH}_2$  group and bond alternation of the carbon backbone. Only while the molecules are near the FC region are their photoelectron spectra expected to be somewhat similar to their nonresonant  $\text{He(I)}$  spectra. Accordingly, we assign the structured  $X$  component as this FC region on the  $S_2$  surface.

At 209 nm, the  $X$  components of all molecules show vibrational resolution in the  $1 + 1'$  (low kinetic energy) region of the photoelectron spectrum (Figure 10). In CR and MVK, a vibrational progression with a spacing of roughly 0.15 eV or  $1200\text{ cm}^{-1}$  is seen. This progression is assigned to  $\text{C}=\text{C}$  stretching in the ionic states of the molecules and matches the previously reported value for CR.<sup>36</sup> At 200 nm, all molecules show the  $\text{C}=\text{C}$  stretch vibrational progression (Figure 11).

**TABLE 4: Fitted Time Constants for TRPES Scans of Acrolein, Crotonaldehyde, Methylvinylketone, and Methacrolein Using 200 nm Pump and 267 nm Probe Wavelengths**

	energy range (eV)	$t_1$ (fs)	$t_2$ (fs)
AC	0.30–0.75	$100 \pm 30$	$620 \pm 80$
	0.75–1.8	$110 \pm 30$	
	1.8–2.6	$75 \pm 25$	
	2.6–5.0	$60 \pm 20$	
CR	0.25–1.12	$70 \pm 25$	$480 \pm 25$
	1.12–2.6	$70 \pm 25$	
	2.6–5.0	$50 \pm 20$	
MVK	0.30–1.2	$170 \pm 40$	$1040 \pm 100$
	1.2–2.0	$190 \pm 30$	
	2.0–2.6	$170 \pm 40$	
	2.6–5.0	$90 \pm 30$	
MA	0.30–0.93	$110 \pm 25$	$1800 \pm 100$
	0.93–2.0	$130 \pm 30$	
	2.0–2.7	$95 \pm 25$	
	2.7–5.0	$70 \pm 20$	

<sup>a</sup> The model used to fit the spectra consisted of a cross-correlation response  $X$ , an immediately excited species  $A$  that decays with time constant  $t_1$  to intermediate  $I$ , which in turn decays with time constant  $t_2$  to product  $P$ .

Once leaving the FC region, the molecules make their way toward the  $S_2/S_1$  conical intersection located roughly 1.5 eV (as calculated by CASSCF) below the  $S_2$  FC region. We propose that the  $A$  signal arises from these molecules still on the  $S_2$  surface but located away from the FC region. From the apparent absence of a true minimum for  $S_2$ , one would expect very rapid internal conversion to  $S_1$ , as seems to be reflected by the short  $A$  lifetimes ( $t_1$ ) in Tables 3 and 4. There are small differences in  $t_1$  between the molecules, with CR being the fastest (50–90 fs), followed by AC (45–110 fs), MA (65–155 fs), and finally MVK (90–190 fs). However, we draw no conclusions from these small differences due to the uncertainties in the fitting procedure as described previously. The differences in  $t_1$  at 200 and 209 nm appear to be minimal, suggesting that similar dynamics are occurring on the  $t_1$  time scale at both wavelengths for all molecules. For all of the enones, the  $t_1$  decay times at low photoelectron kinetic energies are longer compared to those at higher kinetic energies. Spectrally, this means that the photoelectron spectrum of  $A$  is shifting to lower kinetic energies as time progresses. Correspondingly, this means that the excited molecules preferentially ionize to more highly excited vibrational states at later times. This observation is indicative of large deformations (bond stretching and torsion) occurring on the  $S_2$  surface.

After passing through the  $S_2/S_1$  conical intersection, the molecules reside on the  $S_1$  surface. This is component  $I$  in our model, with its lifetime described by  $t_2$ . By referring to Tables 3 and 4, we come to the most striking observation that the  $t_2$  relaxation times are very different for the different  $\alpha,\beta$ -enones. At 209 nm, CR (360–560 fs) appears to have the fastest  $t_2$  relaxation time by a factor of  $\sim 2$  compared to AC ( $900 \pm 100$  fs) and MVK ( $1080 \pm 80$  fs), while MA ( $2020 \pm 80$  fs) is the slowest by a factor of  $\sim 2$ . At 200 nm, AC ( $615 \pm 80$  fs) and MA ( $1800 \pm 100$  fs) speed up slightly, while CR ( $480\text{--}580$  fs) and MVK ( $1040 \pm 100$  fs) stay approximately the same, as compared to their relaxation times at 209 nm.

Three possibilities exist for relaxation from the  $S_1$  state: fluorescence from  $S_1$ , ISC to the triplet manifold, or decay through a conical intersection to the ground state  $S_0$ . From the short lifetimes of the  $S_1$  states, fluorescence can be ruled out.

Intersystem crossing as the major relaxation pathway remains somewhat dubious, as it seems unlikely that a spin-forbidden process can compete with spin-allowed internal conversion. Thus, we conclude that the dominant  $S_1$  relaxation pathway is rapid decay through the  $S_1/S_0$  conical intersection.

The significance of differences in the  $S_1$  decay times for the enones is supported by HCO(X) quantum yield measurements on AC and CR photolysis at 193 nm.<sup>42</sup> Using laser-induced fluorescence, HCO ground-state photoproducts, HCO(X), thought to be formed exclusively via the triplet manifold,<sup>11,25</sup> were observed only from AC, while no detectable production (<0.35%) was found from CR. (The observation of triplet products does not contradict the statement that ISC may not be the major relaxation pathway because the singlet–triplet branching ratios are not known.) With the addition of the methyl group, the rate of ISC for CR might be expected to be greater or equal to that of AC, depending on whether or not the methyl group increases the local density of states through coupling to the mode promoting ISC. In contradiction, the entire triplet yield seems to be shut off by the addition of the methyl group. Two explanations are possible: (1) the opening of another channel on the  $S_1$  surface in CR that depletes the  $S_1$  population or (2) remarkably faster internal conversion in CR via the  $S_1/S_0$  conical intersection as compared to AC.

The accessibility of a new channel in CR cannot be excluded by energetic reasons because fragmentation to produce the excited-state fragment HCO(A) is possible at wavelengths used in our TRPES experiments. The 193 nm photolysis experiments<sup>42</sup> were only able to detect ground-state HCO(X) not HCO(A). Experiments using synchrotron vacuum UV light as the ionization source following 193 nm excitation<sup>27</sup> speculate that this channel might be present. However, direct observation of the HCO(A) photoproduct is impossible because it is unstable relative to further fragmentation. There are a number of drawbacks for this explanation of the observed  $S_1$  relaxation times. A barrier restricts HCO(A) formation in AC.<sup>11</sup> Thus, this explanation requires the unlikely result that simple addition of the methyl group at the end of AC substantially lowers the barrier to HCO(A) formation. Also, by Hammond’s postulate, one would expect that corresponding formation of the more stable acetyl radical  $\text{CH}_3\text{CO}$  from MVK would be more favorable and should have a shorter  $S_1$  relaxation time than CR, which it does not. In addition, this mechanism cannot explain why the  $S_1$  relaxation time is slower for MA.

The more probable explanations for the differing  $S_1$  decay times between the enones are differences occurring at or near the  $S_1/S_0$  conical intersection, resulting in promotion or retardation of internal conversion to the ground state. We attempted to find correlations between the  $S_1$  decay times and the properties defining the CI. Table 5 shows the computed values for the barrier  $E^\ddagger$  (difference between the  $S_1$  minimum and the  $S_1/S_0$  MECI), the total excess energy  $E_{\text{xs}}$  (difference between  $S_2$  FC and  $S_1/S_0$  MECI), and the excess averaged over the number of modes,  $E_{\text{xs,avg}}$ , for each of the four molecules. From these values, it is clear that energetics alone cannot explain the difference in  $S_1$  lifetimes—it fails to discriminate between CR, MVK, and MA (whose lifetimes differ by a factor of 2) and would dictate that AC decays faster than CR (which it does not).

Next, we examined the topographical features of the  $S_1/S_0$  intersection itself. For the case of a two-state crossing, in the two coordinates that break the degeneracy, the potential energy surfaces resemble a double cone with the CI at the apex. Far from being mere isolated points, CIs form  $(N - 2)$ -dimensional

**TABLE 5: Calculated Properties near the  $S_1/S_0$  Conical Intersections for the  $\alpha,\beta$ -Enones Discussed Here<sup>a</sup>**

	AC	CR	MVK	MA
$E^\ddagger$ (eV)	0.98	0.99	0.82	0.82
$E_{\text{xs}}$ (eV)	3.61	3.03	3.23	3.16
$E_{\text{xs,avg}}$ (eV)	0.20	0.11	0.12	0.12
$s_x$	0.083	0.083	0.065	0.089
$s_y$	0.0000	0.0000	0.0001	0.0000
$d_{gh}$	0.021	0.021	0.018	0.022
$\Delta_{gh}$	0.952	0.953	0.893	0.956
$t_2^{209 \text{ nm}}$ (fs)	900	400	1080	2020

<sup>a</sup>  $E^\ddagger$  is the energy between the  $S_1$  minimum and the  $S_1/S_0$  MECI.  $E_{\text{xs}}$  is the excess energy available at the  $S_1/S_0$  MECI (i.e., the energy difference between  $S_2$  FC and  $S_1/S_0$  MECI).  $E_{\text{xs,avg}}$  is the excess energy averaged over the number of vibrational modes. Projections of the gradient difference (**g**) and nonadiabatic coupling (**h**) vectors onto the seam gradient vector (**s**) are given by  $s_x$  and  $s_y$ , respectively.  $d_{gh}$  represents the distance metric in the branching space, and  $\Delta_{gh}$  represents the asymmetry of the conical intersection.  $t_2^{209 \text{ nm}}$  are the measured  $S_1$  decay times from the TRPES experiments.

seams along which two (and possibly three,<sup>41,43</sup> in which case the seam is  $N - 5$  dimensional) electronic states are degenerate. The two dimensions along which the degeneracy is broken form the branching,<sup>4</sup> or **g**–**h**<sup>44</sup> plane. We begin by considering two electronic states  $|I\rangle$  and  $|J\rangle$  with energies  $E_I(\mathbf{R})$  and  $E_J(\mathbf{R})$ , respectively. The **g** (gradient difference) vector is defined by

$$2\mathbf{g}_{IJ} = \nabla_{\mathbf{R}}(E_I(\mathbf{R}) - E_J(\mathbf{R})) \quad (6)$$

in which the  $\nabla_{\mathbf{R}}$  operator indicates differentiation with respect to nuclear coordinates, all of which have been appropriately mass-weighted. Likewise, the nonadiabatic coupling vector **h** between electronic states  $|I\rangle$  and  $|J\rangle$  is defined as

$$\mathbf{h}_{IJ} = \langle I | \nabla_{\mathbf{R}} | J \rangle (E_I - E_J) = \langle I | \nabla_{\mathbf{R}} H | J \rangle \quad (7)$$

The classification of conical intersections as “peaked” or “sloped” is based on the projections

$$s_x = \mathbf{s} \cdot \mathbf{x} \quad (8)$$

$$s_y = \mathbf{s} \cdot \mathbf{y} \quad (9)$$

in which **x** and **y** are normalized versions of the branching plane vectors **g** and **h**, respectively

$$\mathbf{x} = \frac{\mathbf{g}}{||\mathbf{g}||} \quad (10)$$

$$\mathbf{y} = \frac{\mathbf{h}}{||\mathbf{h}||} \quad (11)$$

The seam coordinate **s** is

$$2\mathbf{s} = \nabla_{\mathbf{R}}(E_I(\mathbf{R}) + E_J(\mathbf{R})) \quad (12)$$

representing the gradient of the average energy of the intersection seam.

In addition to the projections, two additional parameters are needed to fully characterize the seam space.<sup>45</sup> The first of these

$$\Delta_{gh} = \frac{||\mathbf{g}||^2 - ||\mathbf{h}||^2}{||\mathbf{g}||^2 + ||\mathbf{h}||^2} \quad (13)$$

measures the intersection asymmetry, or ellipticity of the intersection. The final parameter

$$d_{gh} = \sqrt{||\mathbf{g}||^2 + ||\mathbf{h}||^2} \quad (14)$$

provides a distance metric for the branching space. Larger values of  $d_{gh}$  represent steeper pitched (narrower) CIs than smaller values.

The branching plane ( $\mathbf{g}$  and  $\mathbf{h}$ ) vectors as determined by standard intersection optimization schemes are unique only to within arbitrary rotations, and their orthogonality is generally not guaranteed. Because the magnitudes of  $s_x$  and  $s_y$  vary with the rotation of  $\mathbf{g}$  and  $\mathbf{h}$ , these vectors must be phased in a unique and consistent fashion for the projections to have unambiguous significance. As Yarkony has shown previously,<sup>3</sup> this difficulty can be removed by forcing orthogonality of the original pair. This, in turn, can be achieved by linear transformation to new  $\bar{\mathbf{g}}$  and  $\bar{\mathbf{h}}$

$$\bar{\mathbf{g}}^U = (\mathbf{g}^U \cos 2\beta + \mathbf{h}^U \sin 2\beta) \quad (15)$$

$$\bar{\mathbf{h}}^U = (\mathbf{h}^U \cos 2\beta - \mathbf{g}^U \sin 2\beta) \quad (16)$$

The rotation angle  $\beta$  is calculated from

$$\tan 4\beta = \frac{2[\mathbf{h}^U \cdot \mathbf{g}^U]}{[||\mathbf{h}^U||^2 - ||\mathbf{g}^U||^2]} \quad (17)$$

This particular rotation of the branching space has several pleasant consequences, including assurance that  $\bar{\mathbf{g}}^U$  and  $\bar{\mathbf{h}}^U$  reflect the point group symmetry of the molecule and are continuous along the intersection seam.

Previous studies<sup>3,4</sup> attempted to correlate intersection topography with decay efficiency, and we summarize the relevant points here. Intersections with branching plane vectors having zero projection ( $s_x = 0$ ,  $s_y = 0$ ) onto the seam coordinate are described as vertical or “peaked” cones. In this situation, the upper surface lies entirely above the CI in energy, while the lower surface lies entirely below. This topography conforms closely to the classical picture of a funnel, meaning that population on the upper state is very efficiently directed to and through the intersection located at the apex of the cone. Intersections with branching space axes having nonzero projection onto the seam coordinate ( $s_x \neq 0$  and/or  $s_y \neq 0$ ), however, are tilted or “sloped”. In this case, the cone axis can be tilted significantly such that parts of the upper surface lie below the CI energy while parts of the lower surface lie above the CI energy. Some trajectories pass efficiently through these sloped CIs, while others do not. In addition, recrossing of the CI is possible for such geometries. More so than in the peaked pattern, the direction by which a sloped CI is approached can be critical in determining whether the adiabatic or nonadiabatic pathway is followed. The symmetry and pitch of the CI, defined by  $\Delta_{gh}$  and  $d_{gh}$ , can also affect the efficiency of passage through the CI.

The parameters defining the conical intersections are illustrated with two examples shown in Figure 14. Figure 14a shows two views of a vertical asymmetric CI. A nonzero  $\Delta_{gh}$  is readily seen as a difference in slopes of the PESs along the  $\mathbf{g}$  and  $\mathbf{h}$  vectors. The projections of the seam coordinate ( $\mathbf{s}$ ) onto the branching space vectors are zero, and the cone axis is completely vertical. Figure 14b shows two views of a symmetric sloped CI, whose cone axis is only tilted along the gradient difference vector  $\mathbf{g}$ . The CI is not tilted along the nonadiabatic coupling vector  $\mathbf{h}$ ; thus only  $s_x \neq 0$  and  $s_y = 0$ . The CI is

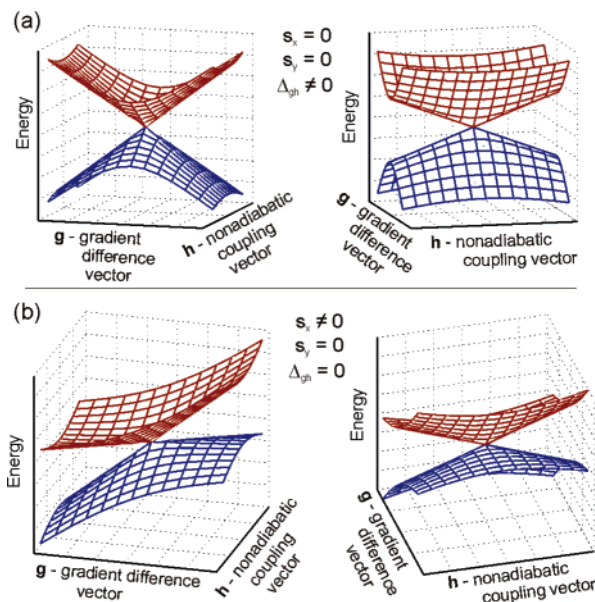


**Figure 14.** Examples of conical intersections in the space defined by the gradient difference  $\mathbf{g}$  and nonadiabatic coupling  $\mathbf{h}$  vectors. The upper and lower surfaces are red and blue, respectively. The left and right diagrams are different views of the same intersection. (a) An asymmetric, peaked conical intersection. The asymmetry, parametrized by  $\Delta_{gh}$ , is easily seen as the differing slopes along the  $\mathbf{g}$  and  $\mathbf{h}$  vectors near the intersection.  $s_x = s_y = 0$  indicates that the cone axis is vertical. (b) A symmetric, sloped intersection.  $s_x \neq 0$  and  $s_y = 0$  indicate that the cone axis is only tilted along the  $\mathbf{g}$  direction.

symmetric because  $\Delta_{gh}$  is zero. Unlike the idealized examples presented here, real conical intersections in general contain some degree of both tilt and asymmetry. It is important to note that the preceding parametrization of conical intersections describes only a local PES subspace near the CI. Generalizations as to the size of this linear region are quite difficult to make. Larger global PES features (barriers and valleys) may play more important roles in CI accessibility.

The gradient difference  $\mathbf{g}$  and nonadiabatic coupling  $\mathbf{h}$  vectors for AC are shown in Figure 15. The gradient difference vector is mostly bond alternation of the nominal C–C bond, but due to motions of the aldehyde H and O, it bears resemblance to scissoring motion of the CCOH. The nonadiabatic coupling vector is pyramidalization of the central backbone carbon. The  $\mathbf{g}$  and  $\mathbf{h}$  vectors for CR, MVK, and MA are qualitatively the same as those for AC, providing no evidence to explain the differences in  $S_1$  lifetimes between the molecules. The displacement vectors for  $\mathbf{g}$ ,  $\mathbf{h}$ , and  $\mathbf{s}$  are included in the Supporting Information.

In Table 5, we show the calculated the parameters  $s_x$ ,  $s_y$ ,  $\Delta_{gh}$ , and  $d_{gh}$  describing the topography of the  $S_1/S_0$  CIs for the  $\alpha,\beta$ -enones. The results reveal intersections sloped sharply along the gradient difference axis but almost perfectly peaked along that of the nonadiabatic coupling ( $s_y \approx 0$ ). Qualitatively, they resemble the CI presented in Figure 14b. The calculated PES landscape for AC is shown in Figure 16. The values of  $s_x$  differ by <10% between the molecules. Assuming approach of the  $S_1/S_0$  MECI from the  $S_1$  minimum (i.e., from below the CI), the magnitudes of  $s_x$  fail to distinguish between AC and CR, and values for both are larger than that for MVK, even though their  $t_2$  decay rates are higher. This is contrary to the correlation anticipated by Yarkony.<sup>3</sup> Lack of a clear pattern relating the  $\mathbf{s}$  projection values with  $t_2$  is perhaps not surprising in this context because the relative differences in tilt and asymmetry examined here are quite small in comparison to those studied previously<sup>3</sup> (in which they are greater than 0.5 for both  $s_x$  and  $\Delta_{gh}$ ).



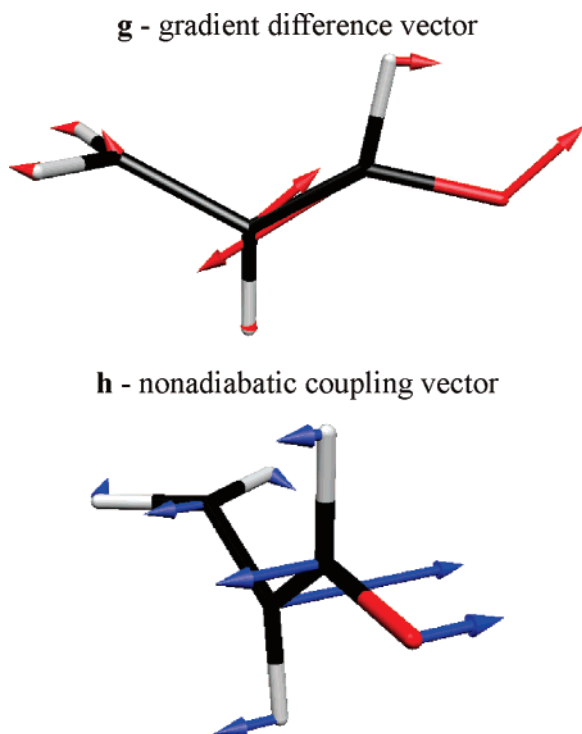


**Figure 15.** Gradient difference and nonadiabatic coupling vectors for acrolein. The gradient difference vector is essentially bond alternation (strongest on the nominally C–C bond) but due to motions of the aldehyde H and O bears some resemblance to scissoring motion of the CCOH. The nonadiabatic coupling vector is pyramidalization of the central backbone carbon.

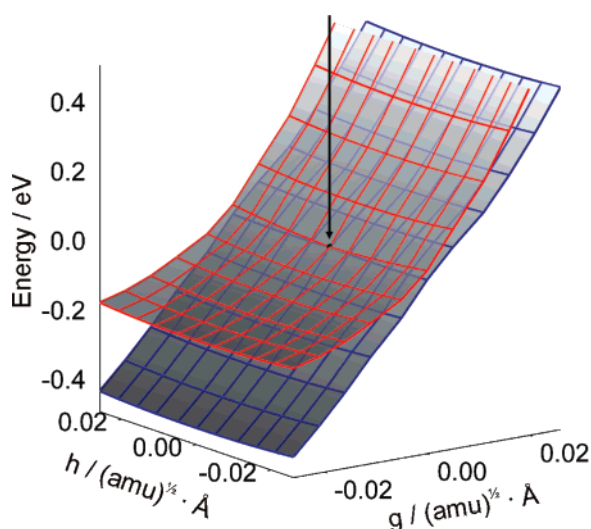


**Figure 16.** SA3-CAS(6,5)/6-31G\* potential energy surfaces in the neighborhood of the  $S_1/S_0$  minimal energy conical intersection in acrolein. The intersection point is marked by an arrow, and comparison of the grid lines reveals that the degeneracy is broken much more rapidly along the gradient difference (**g**) axis than along that of the nonadiabatic coupling (**h**).

The CIs for the molecules are also quite asymmetric, as indicated by the values of  $\Delta_{gh}$  in Table 5 and shown in Figure 16. The intersections all are steeply sloped along the gradient difference vectors while the degeneracy is barely broken along the nonadiabatic coupling vector. Again there do not appear to be appreciable differences in the CI asymmetries that would explain trends seen in the  $S_1$  relaxation behavior.

The analysis thus far has dealt with static features on the potential energy surfaces of the molecules and the energies and

topographies of the conical intersections. It fails to find a consistent explanation for the observed differences in relaxation rates between the four molecules. Therefore, the remaining important issues are the vibrational dynamics occurring near the  $S_1/S_0$  CI and their relationship to surface crossing probabilities. The geometric changes required to move from the  $S_1$  minimum to the  $S_1/S_0$  MECI are dominated by torsion about the terminal  $\text{CH}_2$  (or  $\text{CHCH}_3$  in CR). It is here where we point out an important dynamical effect that potentially explains the different  $S_1$  relaxation time scales between CR and the other  $\alpha,\beta$ -enones. Due to the presence of the methyl group on CR, torsion about the terminal  $\text{CHX}$  methylene group is expected to be approximately twice as slow compared to that in AC, MVK, and MA.

This leads us to propose a mechanism for the faster internal conversion in CR. Vertically oriented CIs funnel the trajectories toward the intersection to promote fast internal conversion. However, the direction of approach is important in determining the efficiency of crossing in sloped CIs. As indicated above, the  $S_1/S_0$  MECIs for all of the enones are of this latter type. Figure 9 indicates that the MECI geometries for the molecules are all twisted  $\sim 90^\circ$  about the terminal  $-\text{C}=\text{CHX}$ . A complete rotation about the methylene bond takes the trajectory from the  $S_1$  minimum at  $0^\circ$  and  $180^\circ$  (planar geometry) to regions nearby the  $S_1/S_0$  CI at  $90^\circ$  and  $270^\circ$  (twisted geometry). We speculate that slow torsion through the CI region promotes internal conversion. In CR, more time is spent near the intersection region on each pass near the CI region, during which other molecular motions can occur. Importantly, these motions can bring the molecular trajectory to the  $S_1/S_0$  CI, resulting in rapid internal conversion to the ground state. Conversely, for the faster twisting molecules (AC, MVK, and MA), the trajectories pass through the CI region relatively quickly, missing the opportunity to pass through the CI. Interestingly, this postulate is opposite in nature to the analysis of one-dimensional Landau–Zener avoided crossings, where faster moving trajectories are more likely to follow the diabatic pathway to end up on the other surface, while slower moving trajectories follow the adiabatic pathway and remain on the same surface. However, this difference in behavior is not surprising considering that for CIs the upper and lower surfaces do meet at a degenerate point, unlike the case in avoided crossings. We also point out that this torsion is not one of the two coordinates that lifts the degeneracy in first order at the MECI. However, it is important to note that the branching plane coordinates have a privileged role in altering the energy gap between states only in a limited region around the MECI—the region where the cone is well-described by a first-order Hamiltonian. In the present molecules, the region encompassing the relevant dynamics extends beyond the linear region, and one must also consider the role of the seam coordinates in altering the energy gap, even though their effect is only second order at the MECI. The torsion is one of these seam coordinates.

While faster rotation of the  $\text{CH}_2$  group is consistent with the relatively longer  $S_1$  decay times observed for AC and MVK, we note that of MA appears anomalously long. With a similar torsional frequency about the terminal  $\text{CH}_2$  bond, the reasons outlined above would predict MA to have a similar  $S_1$  decay time as compared to those of AC and MVK. However, this is not the case. For MA, we propose a different effect responsible for the slower  $S_1$  relaxation dynamics. Examination of the branching space vectors for AC in Figure 15 reveals that the nonadiabatic coupling vector (**h**) is primarily pyramidalization around the central carbon. The magnitude and speed of the



motion of this carbon are affected by substitution of the hydrogen with a relatively heavy methyl group at this location, as is the case in MA. As such, the **h** motion in MA is expected to be slower relative to that in CR, AC, and MVK. A key difference in this situation compared to the anomalous decay rate in CR is the fact that the methyl group in MA is directly affecting one of the branching space vectors (in this case **h**). We expect that MA, AC, and MVK access the intersection region, with the terminal methylene group twisted by 90°, at approximately the same rate. We speculate that AC and MVK have overall faster  $S_1$  relaxation because the molecules are moving faster along the directions described by the **g** and **h** vectors, which allow them to access the  $S_1/S_0$  CI more efficiently than MA.

We postulate that the relative speeds of specific motions are important in controlling relaxation rates in sloped conical intersections. Motions that are required to reach the CI, but are not necessarily responsible in first order for creating the intersection (e.g., the torsional mode), speed up the crossing rate (as in CR). Conversely, motions that create the intersection (i.e., the **g** and **h** vectors) speed up the crossing rate when they are fast because they quickly shoot the trajectory through the CI. This reasoning seems consistent with the experimentally observed trend in  $S_1$  relaxation rates. CR has the fastest decay because both effects, slow torsional motion to reach the CI region and fast motion along the **h** coordinate, drive nonadiabatic crossing. At the other extreme in decay rates, MA is the slowest because both effects, fast torsional motion by the CI region and slow motion along the **h** coordinate, are detrimental to nonadiabatic crossing. AC and MVK fall in between because the effects operate in a canceling fashion, with fast torsional motion retarding relaxation and fast motion along the **h** coordinate promoting relaxation. We stress that this analysis applies only to sloped conical intersections where the excited-state trajectories are expected to come from points on the PES lower in energy.

Clearly, more experimental and theoretical investigations are needed to explore the validity of the postulates presented here. Attempts to theoretically clarify these issues using full quantum mechanical dynamics calculations are currently underway.

#### 4. Conclusion

We measured the ultrafast dynamics of the  $\alpha,\beta$ -enones acrolein (AC), crotonaldehyde (CR), methylvinylketone (MVK), and methacrolein (MA) after excitation to the  $S_2$  electronic surface at 200 and 209 nm. The molecules initially move quickly away from the Franck–Condon overlap region toward their respective  $S_2$  minima. Large-amplitude motions are observed as they make their way toward  $S_2/S_1$  conical intersections to land on the  $S_1$  state roughly 50–200 fs later. The molecules then pass through another conical intersection to the ground state. Intersystem crossing to the triplet manifold is believed to be minimal and is not considered further here. Small differences between the molecules are seen in the  $S_2$  relaxation times. However, large differences are seen in the  $S_1$  relaxation times, with CR decaying the quickest, followed by AC and MVK approximately equal, and MA considerably slower. Thus, the  $S_1$  decay dynamics are greatly affected by the position of the methyl group substituent. Ab initio calculations of the geometries, topographies, and  $S_1/S_0$  minimal energy conical intersections (MECIs) do not reveal reasons for the observed differences. We conclude that dynamical factors (i.e., motions of the atoms on the potential energy surface) play a large role in the  $S_1$  decay rates through the sloped  $S_1/S_0$  conical intersections.

We propose a model in which the speeds of specific motions in the molecules affect their nonadiabatic crossing rate. We

identify two important types of motions in the molecules that we studied. The molecular displacements described by the **g** and **h** vectors lift the electronic degeneracy in first order around the MECI. Displacements in this “branching plane” play a role analogous to the single coordinate in Landau–Zener models. Increased momentum in the branching coordinates leads to more efficient nonadiabatic transitions and thus faster decay. The  $N - 2$  remaining molecular displacements lift the degeneracy only in second or higher order around the MECI. Thus, these “complementary coordinates”, also known as “seam coordinates”, are of less relevance in promoting the nonadiabatic transition itself. However, motion in the complementary coordinates controls access to the MECI region. The longer the molecule is in the MECI region, the more chance it has to undergo displacement along the branching coordinates to make a nonadiabatic transition. Hence, increased momentum in the complementary coordinates decreases the amount of time spent in the MECI region each time it is accessed. This leads to a slower decay—the opposite of the momentum dependence that is predicted for the branching coordinates.

In the case of the  $\alpha,\beta$ -enones, the most important complementary coordinate is the terminal methylene torsion. This torsion is one of the largest distortions proceeding from the  $S_1$  minimum to the  $S_1/S_0$  MECI. However, it is not one of the branching coordinates and therefore does little to promote nonadiabatic transitions. A 90° twisting in this coordinate is required to reach the vicinity of the intersection seam—this is a necessary but not a sufficient condition for nonadiabatic transitions. One further requires distortions of the branching coordinates for efficient population decay. This reasoning is consistent with the measured  $S_1$  relaxation rates in the  $\alpha,\beta$ -enones. CR has the fastest decay because it has the slowest methylene torsion and also fast motion of the **g** and **h** vectors. AC and MVK are of an intermediate decay rate because the effects of the fast methylene torsion and fast CI modes oppose each other. MA has the slowest decay rate because it has fast methylene torsion and the methyl group substituent slows **h**.

**Acknowledgment.** A.M.D.L. acknowledges support from NSERC PGSB and NRC GSSSP grants. This work was supported in part by the National Science Foundation (Grant Nos. CHE-05-35640 and CHE-02-11876).

**Supporting Information Available:** Additional figures as mentioned in the text. This material is available free of charge via the Internet at <http://pubs.acs.org>.

#### References and Notes

- (1) Bernardi, F.; Olivucci, M.; Robb, M. A. *Pure Appl. Chem.* **1995**, *67*, 17–24.
- (2) Ben-Nun, M.; Martinez, T. J. *Chem. Phys.* **2000**, *259*, 237–248.
- (3) Yarkony, D. R. *J. Chem. Phys.* **2001**, *114*, 2601–2613.
- (4) Atchity, G. J.; Xantheas, S. S.; Ruedenberg, K. *J. Chem. Phys.* **1991**, *95*, 1862.
- (5) Landau, L. D. *Phys. Z. Sowjetunion* **1932**, *2*, 46.
- (6) Zener, C. *Proc. R. Soc. London, Ser. A* **1932**, *137*, 696.
- (7) Blanchet, V.; Zgierski, M. Z.; Seideman, T.; Stolow, A. *Nature* **1999**, *401*, 52.
- (8) Stolow, A. *Annu. Rev. Phys. Chem.* **2003**, *54*, 89.
- (9) Stolow, A.; Bragg, A. E.; Neumark, D. M. *Chem. Rev.* **2004**, *104*, 1719.
- (10) Reguero, M.; Olivucci, M.; Bernardi, F.; Robb, M. A. *J. Am. Chem. Soc.* **1994**, *116*, 2103–2114.
- (11) Fang, W.-H. *J. Am. Chem. Soc.* **1999**, *121*, 8376–8384.
- (12) Page, C. S.; Olivucci, M. *J. Comput. Chem.* **2003**, *24*, 298–309.
- (13) Birge, R. R.; Leermakers, P. A. *J. Am. Chem. Soc.* **1972**, *94*, 8105–8117.
- (14) Aquilante, F.; Berone, V.; Roos, B. O. *J. Chem. Phys.* **2003**, *119*, 12323–12334.

- (15) Brand, J. C. D.; Williamson, D. G. *Discuss. Faraday Soc.* **1963**, 35, 184–191.
- (16) Hollas, J. M. *Spectrochim. Acta* **1963**, 19, 1425–1441.
- (17) Inuzuka, K. *Bull. Chem. Soc. Jpn.* **1961**, 34, 729–732.
- (18) Osborne, G. A.; Ramsay, D. A. *Can. J. Phys.* **1973**, 51, 1170–1175.
- (19) Paulisse, K. W.; Friday, T. O.; Graske, M. L.; Polik, W. F. *J. Chem. Phys.* **2000**, 113, 184–191.
- (20) Birge, R. R.; Pringle, W. C.; Leermakers, P. A. *J. Am. Chem. Soc.* **1971**, 93, 6715–6726.
- (21) Shinohara, H.; Nishi, N. *J. Chem. Phys.* **1982**, 77, 234–245.
- (22) El-Sayed, M. A. *J. Chem. Phys.* **1963**, 38, 2834–2838.
- (23) Fujimoto, G. T.; Umstead, M. E.; Lin, M. C. *J. Chem. Phys.* **1985**, 82, 3042–4044.
- (24) Haas, B. M.; Minton, T. K. M.; Felder, P.; Huber, J. R. *J. Phys. Chem.* **1991**, 95, 5149–5159.
- (25) Kao, Y.-T.; Chen, W.-C.; Yu, C.-H.; Chen, I.-C. *J. Chem. Phys.* **2001**, 114, 8964–8970.
- (26) Parsons, B. F.; Szpumar, D. E.; Butler, L. J. *J. Chem. Phys.* **2002**, 117, 7889–7885.
- (27) Shu, J.; Peterka, D. S.; Leone, S. R.; Ahmed, M. *J. Phys. Chem. A* **2004**, 108, 7895.
- (28) Jen, S.-H.; Chen, I.-C. *J. Chem. Phys.* **1999**, 111, 8448–8453.
- (29) Johnstone, D. E.; Sodeau, J. R. *J. Chem. Soc., Faraday Trans.* **1992**, 88, 409–415.
- (30) Loison, J.-C.; Kable, S. H.; Houston, P. L. *J. Chem. Phys.* **1991**, 94, 1796–1802.
- (31) Fahr, A.; Braun, W.; Laufer, A. H. *J. Phys. Chem.* **1993**, 97, 1502–1506.
- (32) Pola, J.; Koga, Y.; Ouchi, A. *Tetrahedron* **1997**, 53, 3757–3766.
- (33) Lochbrunner, S.; Larsen, J.; Shaffer, J.; Schmitt, M.; Schultz, T.; Underwood, J.; Stolow, A. *J. Electron Spectrosc. Relat. Phenom.* **2000**, 112, 183–198.
- (34) Masclet, P.; Mouvier, G. *J. Electron. Spectrosc. Relat. Phenom.* **1978**, 14, 77–97.
- (35) Tam, W.-C.; Yee, D.; Brion, C. E. *J. Electron. Spectrosc. Relat. Phenom.* **1974**, 4, 77–80.
- (36) van Dam, H.; Oskam, A. *J. Electron. Spectrosc. Relat. Phenom.* **1978**, 13, 273–290.
- (37) Roos, B. O. The complete active space self-consistent field method and its applications in electronic structure calculations. In *Ab Initio Methods in Quantum Chemistry II*; Lawley, K. P., Ed.; Advances in Chemical Physics 69; Wiley: New York, 1987; p 399.
- (38) Docken, K. K.; Hinze, J. *J. Chem. Phys.* **1972**, 57, 4928–4936.
- (39) Werner, H.-J.; Knowles, P. J.; Amos, R. D.; Bernhardsson, A.; Berning, A.; Celani, P.; Cooper, D. L.; Deegan, M. J. O.; Dobbyn, A. J.; Eckert, F.; Hampel, C.; Hetzer, G.; Korona, T.; Lindh, R.; Lloyd, A. W.; McNicholas, S. J.; Manby, F. R.; Meyer, W.; Mura, M. E.; Nicklass, A.; Palmieri, P.; Pitzer, R.; Rauhut, G.; Schutz, M.; Schumann, U.; Stoll, H.; Stone, A. J.; Tarroni, R.; Thorsteinsson, T. *MOLPRO*, 2002.
- (40) Quenneville, J.; Martinez, T. *J. Phys. Chem. A* **2003**, 107, 829–837.
- (41) Coe, J. D.; Martinez, T. *J. Phys. Chem. A* **2006**, 110, 618–630.
- (42) Gessner, O.; Chrysostom, E. T. H.; Lee, A. M. D.; Wardlaw, D. M.; Ho, M. L.; Lee, S. J.; Cheng, B. M.; Zgierski, M. Z.; Chen, I. C.; Shaffer, J. P.; Hayden, C. C.; Stolow, A. *Faraday Discuss.* **2004**, 127, 193–212.
- (43) Matsika, S.; Yarkony, D. R. *J. Chem. Phys.* **2002**, 117, 6907–6910.
- (44) Yarkony, D. *J. Phys. Chem. A* **1997**, 101, 4263–4270.
- (45) Yarkony, D. R. *J. Chem. Phys.* **2000**, 112, 2111–2120.